

# Relaxation and Short Time Dynamics of Bulk Liquids and Fluids Confined in Spherical Cavities and Slit Pores

S. H. Krishnan and K. G. Ayappa\*

Department of Chemical Engineering, Indian Institute of Science, Bangalore-India 560012

Received: August 7, 2005; In Final Form: September 30, 2005

The density of states for bulk and confined fluids have been modeled using a recently proposed  $\gamma$  distribution (Krishnan, S. H.; Ayappa, K. G. *J. Chem. Phys.* **2004**, *121*, 3197). The  $\gamma$  distribution results in a closed form analytical expression for the velocity autocorrelation function and the relaxation time of the fluid. The two parameters of the  $\gamma$  distribution are related analytically to the second and fourth frequency moments of the fluid using short time expansions. The predictions by the proposed  $\gamma$  model are compared with the velocity autocorrelation functions obtained using the theory of instantaneous normal modes (INMs) and from molecular dynamics simulations. The model is applied to a bulk soft sphere liquid and fluids confined in a spherical cavity and slit-shaped pores. The  $\gamma$  model is able to capture the resulting changes in relaxation time due to changes in density and temperature extremely well for both the bulk liquid and confined inhomogeneous fluid situations. In all cases, the predictions by the  $\gamma$  model are superior to those obtained from the INM theory. In the case of the fluid confined in a slit pore, the loadings were obtained from a grand canonical Monte Carlo simulation where the pore is equilibrated with a bulk fluid. This is similar to a confinement situation in a surface force apparatus. The predicted relaxation times vs pore widths from the  $\gamma$  model are seen to accurately capture the oscillations due to formation and disruption of layers within the slit pore.

## 1. Introduction

Understanding the dynamics of dense inhomogeneous fluids that arise due to confinement is important in many industrial processes such as adsorption, catalysis, gas separations, transport in porous materials, and lubrication. Developing a theory for transport under molecular confinement is further complicated by the lack of a complete theory for liquid-state dynamics. The dynamics of a dense liquid can be classified into processes that govern the short time relaxation where the dynamics is dominated by binary collisions. At longer times, the dynamics is dominated by collective effects that are no longer binary in nature, eventually giving rise to the long time diffusive and hydrodynamic limit of the fluid. In this paper, we are concerned with models for the velocity autocorrelation functions (VACFs) and relaxation of the fluid, with particular emphasis on the short and intermediate time dynamics of confined fluids.

Although the harmonic approximation and normal-mode analysis are an appropriate starting point for solids, considerable insight into the dynamics of liquids has been gained by extending these ideas to describe molecular motions in liquids.<sup>1–3</sup> The fundamental idea that liquid-state dynamics can be treated within a harmonic framework has led to the theory of instantaneous normal modes (INMs).<sup>4–7</sup> The INM analysis for a system of interacting particles is carried out by expanding the potential energy of the system up to a quadratic term with respect to any instantaneous configuration. The distribution of frequencies obtained from diagonalizing the Hessian is the INM density of states (DOS). The INM DOS contains both real and imaginary frequencies corresponding to the stable and unstable modes, respectively. The Fourier transform of the DOS yields the VACF of the system. In the time domain, the imaginary

frequencies give rise to a divergent VACF. To obtain a VACF which is not divergent at long times, only the contribution from the real lobe of the DOS is retained.<sup>8</sup> Since the theory of INMs has been developed using a harmonic approximation, it is naturally applicable to studying the short time dynamics of a fluid. By virtue of the harmonic approximation, the theory would appear to be well suited when describing the relaxation of systems such as clusters<sup>9,10</sup> and glasses.<sup>11</sup> INMs have also been used to model the velocity autocorrelation functions of rare gases confined in zeolites,<sup>12,13</sup> and more recently, we have applied INMs to strongly inhomogeneous fluids confined in slit-shaped pores.<sup>14</sup>

While developing theories for the VACF, the models are developed in either the time or frequency domains. INMs fall into the category of frequency domain models where a model for the DOS is developed. The VACF, which lies in the time domain, is related to the power spectrum or the DOS through a Fourier transform. One advantage of developing a model in the frequency domain is that the moments of the DOS, also known as the frequency moments which are equilibrium properties of the fluid, can be obtained from the pair-correlation function of the fluid itself. If a suitable distribution for the DOS is found, then it is possible to relate the parameters of the distribution to the frequency moments of the fluid. The tractability of this approach, however, hinges on the appropriate form of the proposed distribution.<sup>15,16</sup> Following this approach, we have recently proposed a new model for the DOS based on  $\gamma$  distributions.<sup>14</sup> The  $\gamma$  model is developed to predict the short and intermediate time responses of the VACF. The proposition for the  $\gamma$  model originated with the observation that the  $\gamma$  distribution provided an accurate representation of the DOS obtained from the real lobe of the INM theory. The  $\gamma$  model results in a simple analytical expression for the VACF, and the two parameters of the  $\gamma$  model are expressed in terms of the

\* To whom correspondence should be addressed. E-mail: ayappa@chemeng.iisc.ernet.in.

frequency moments of the fluid. When applied to a fluid confined in a slit pore,<sup>14</sup> the short and intermediate time predictions of the VACF were found to be superior to the predictions from the INM theory. A common feature of the model based on  $\gamma$  distributions and the INM theory is that both developments are valid for short and intermediate time dynamics of the fluid and inherently predict a zero diffusivity. However, one is able to extract a reliable estimate of relaxation time for the VACF from these models. In this regard, the predictions of the  $\gamma$  model were found to be superior to the predictions from the INM analysis.

In our first paper<sup>14</sup> where the  $\gamma$  model was introduced, we tested its applicability only for a fluid confined in slit pores at selected pore heights and densities. In this paper, we seek to apply the model to a wider range of conditions, by studying the dynamics of a bulk soft sphere liquid over a wide range of temperatures and two different confinement situations. The first type of confinement involves a fluid within a spherical cavity. Examples of this are fluids encapsulated in micelles and reverse micellar systems. This provides an excellent representation of a nondiffusive system which falls within the purview of both the  $\gamma$  model and the INM analysis and hence serves as a natural choice to test these models. The second confinement situation is the slit pore system which mimics the confinement geometry in the surface force apparatus,<sup>17</sup> where two mica surfaces are in contact with a fluid reservoir. This results in the formation of multiple layers, which alter the dynamics of the confined fluid as the confinement distance is varied. As this process occurs at a fixed chemical potential corresponding to the bulk reservoir, the system is simulated in the grand canonical ensemble. The ensemble averaged number densities from the grand canonical Monte Carlo (GCMC) simulation are used as inputs into a molecular dynamics simulation. In all cases, we compare the predicted DOS, VACFs, and the relaxation times with those obtained from MD simulations. The paper is organized as follows: We first present a brief introduction to the  $\gamma$  model and summarize the key ideas of the INM analysis. Subsequently, we present results for bulk soft sphere liquids and fluids confined in a spherical cavity and slit-shaped pores.

## 2. Theory

The normalized VACF which is the central dynamical quantity of interest in this work is defined as

$$\Psi(t) = \frac{\langle \mathbf{v}(0) \cdot \mathbf{v}(t) \rangle}{\langle |\mathbf{v}(0)|^2 \rangle} \quad (1)$$

where  $\langle |\mathbf{v}(0)|^2 \rangle = 3k_B T/M$ ,  $k_B$  is the Boltzmann constant,  $T$  the temperature, and  $M$  the mass of the diffusing particle. The normalized VACF,  $\Psi(t)$ , and the power spectrum  $\Psi(\omega)$  also referred to as the density of states (DOS) are related with the following Fourier transform pairs

$$\Psi(\omega) = \frac{2}{\pi} \int_0^\infty \cos(\omega t) \Psi(t) dt \quad (2)$$

and

$$\Psi(t) = \int_0^\infty \cos(\omega t) \Psi(\omega) d\omega \quad (3)$$

The above definitions assume that the DOS is normalized, that is,  $\int \Psi(\omega) d\omega = 1$  and  $\Psi(t=0) = 1$  (eq 1). In this paper, the description of  $\Psi(t)$  is based on models for the DOS,  $\Psi(\omega)$ .

One approach is based on INMs, and the other is based on the  $\gamma$  model for the DOS. Both of these approaches are discussed next.

**2.1. Instantaneous Normal Modes.** Since the INM theory has been discussed extensively in the literature,<sup>5,6,8</sup> we briefly present the relevant ideas behind the theory. Consider a collection of  $N$  particles whose total potential energy is  $\mathbf{U}(\mathbf{r}_1, \mathbf{r}_2, \dots, \mathbf{r}_N)$  where  $\mathbf{r}_i$  is the position of the  $i$ th particle. If  $\mathbf{R}(t)$  represents the collective positions of a given configuration at time  $t$ , then the potential energy  $\mathbf{U}$  expanded around a neighboring configuration  $\mathbf{R}(t=0) \equiv \mathbf{R}_0$  is<sup>4</sup>

$$\mathbf{U}(\mathbf{R}) = \mathbf{U}(\mathbf{R}_0) + \mathbf{F}(\mathbf{R}_0) \cdot (\mathbf{R} - \mathbf{R}_0) + (1/2)(\mathbf{R} - \mathbf{R}_0) \cdot \mathcal{H}(\mathbf{R}_0) \cdot (\mathbf{R} - \mathbf{R}_0) \quad (4)$$

where the components of the force vector  $\mathbf{F}(\mathbf{R}_0)$  and Hessian matrix  $\mathcal{H}(\mathbf{R}_0)$  are  $f_i = -(\partial \mathbf{U} / \partial r_i)|_{\mathbf{R}_0}$  and  $h_{ij} = \partial^2 \mathbf{U} / \partial r_i \partial r_j|_{\mathbf{R}_0}$ ,  $i, j = 1, \dots, 3N$ , respectively. The corresponding Hamiltonian for the system

$$H = \sum_{i=1}^{3N} \frac{m_i}{2} \left( \frac{d\mathbf{r}_i}{dt} \right)^2 + \mathbf{U}(\mathbf{R}_0) - \mathbf{F}(\mathbf{R}_0) \cdot (\mathbf{R} - \mathbf{R}_0) + (1/2)(\mathbf{R} - \mathbf{R}_0) \cdot \mathcal{H}(\mathbf{R}_0) \cdot (\mathbf{R} - \mathbf{R}_0) \quad (5)$$

The eigenvalues,  $\omega^2$ , are obtained by diagonalizing the Hessian,  $\mathcal{H}$ , for the system of particles at a particular configuration,  $\mathbf{R}_0$ . Since the system is not in a global potential energy minimum, eigenvalues can be either positive or negative, giving rise to real and imaginary frequencies,  $\omega$ , which represent stable and unstable modes, respectively. The INM DOS is the ensemble or time averaged distribution of frequencies,  $\Psi(\omega)$ , obtained after averaging over many configurations  $\mathbf{R}_0$  during a simulation. A schematic of the INM DOS characteristic of a typical bulk liquid is shown in Figure 1a. The imaginary frequencies are depicted on the negative real axis for convenience. Once  $\Psi(\omega)$  is obtained, the expression for the normalized VACF

$$\Psi(t) = \frac{\int \Psi(\omega) \cos \omega t d\omega}{\int \Psi(\omega) d\omega} \quad (6)$$

If both the real and imaginary frequencies are included while computing  $\Psi(t)$ , then the resulting time-correlation function is divergent at short times. To obtain a  $\Psi(t)$  that is nondivergent, one retains only the contribution from the real lobe of the DOS.<sup>8</sup> This has the following consequences: Since the  $\omega = 0$  intercept of the real lobe of the INM DOS is zero, the model based on the real lobe of the INM predicts a zero diffusivity. It is known that the VACF obtained from the INM DOS is accurate up to the fourth moment only when both lobes of the INM DOS are used.<sup>8</sup> Although the resulting VACF computed from the real lobe is well behaved, neglecting the contributions from the imaginary lobe results in moments that are larger than the actual moments of the system. Hence, VACFs predicted from the real lobe of the INM DOS generally tend to relax faster than the actual VACF.<sup>18</sup>

**2.2. VACF from  $\gamma$  Distribution.** The  $\gamma$  model is based on the proposition<sup>14</sup> that the DOS can be represented by a normalized  $\gamma$  distribution

$$\Psi(\omega) = \frac{\alpha^m}{\Gamma(m)} \omega^{m-1} e^{-\alpha\omega} \quad \text{for } m > 1, \quad \alpha > 0 \quad (7)$$

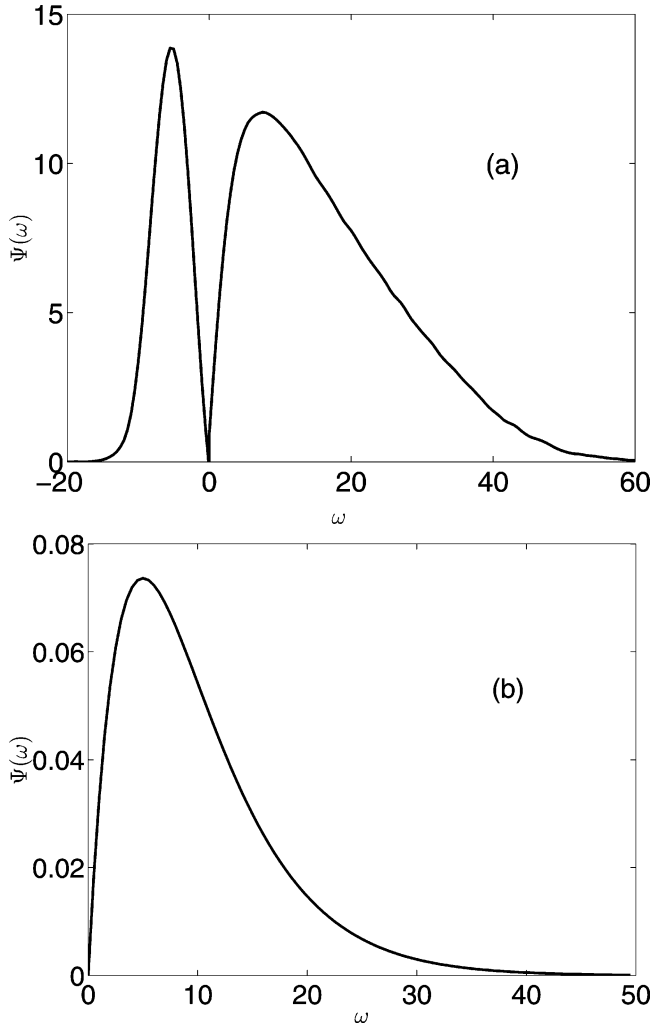


**Figure 1.** Schematic illustrating (a) the INM DOS where the imaginary frequencies are depicted on the negative real axis and (b) the  $\gamma$  distribution. Both the real lobe of the INM DOS and the  $\gamma$  model are zero at  $\omega = 0$  and hence predict a zero diffusivity.

where  $\alpha$  and  $m$  are the two parameters of the model, which are related to the mean,  $m/\alpha$ , and variance,  $m/\alpha^2$ , of the distribution, and  $\Gamma(m)$  is the  $\gamma$  function

$$\Gamma(m) = \int_0^\infty \omega^{m-1} e^{-\omega} d\omega \quad (8)$$

The choice of the  $\gamma$  distribution, illustrated in Figure 1b is motivated by the observation that the distribution captures the essential features that are typically present in distributions obtained from the INM DOS analysis. The distributions are asymmetric about the peak frequency with a long tail toward higher frequencies. The  $\gamma$  distribution is characterized by a power law growth at small frequencies and an exponential decay at large frequencies. Similar to the real lobe of the INM DOS (Figure 1a), the  $\gamma$  model is zero at  $\omega = 0$ . Hence, a model based on the  $\gamma$  distribution for the DOS will predict a vanishing self-diffusion coefficient for the system.

The Fourier transform of the  $\gamma$  distribution results in the following expression for the VACF

$$\Psi(t) = \left[1 + \left(\frac{t}{\alpha}\right)^2\right]^{-m/2} \cos\left[m \arctan\left(\frac{t}{\alpha}\right)\right] \quad (9)$$

$\Psi(t)$  is an even function of time, satisfying the time reversal property of the VACF. The property that the VACF is an even

function of time is a consequence of the definition (eq 3) being a cosine transform and is independent of the choice of  $\Psi(\omega)$ . As a consequence, all odd moments of the VACF vanish at the origin.

**2.3. Parameters for the  $\gamma$  Model.** Since the VACF is an even function of time,<sup>19,20</sup> the Taylor's series expansion around  $t = 0$  is

$$\Psi(t) = 1 - \frac{t^2}{2!} \omega_v^2 + \frac{t^4}{4!} \omega_v^4 - \dots \quad (10)$$

where

$$\omega_v^{2n} = (-1)^n \left( \frac{d^{2n} \Psi(t)}{dt^{2n}} \right)_{t=0} \quad n = 1, 2, \dots \quad (11)$$

are known as the frequency moments. By the use of a series expansion for  $\cos \omega t$ , eq 3 for the VACF can be expressed as

$$\Psi(t) = 1 - \frac{t^2}{2!} \int_0^\infty \Psi(\omega) \omega^2 d\omega + \frac{t^4}{4!} \int_0^\infty \Psi(\omega) \omega^4 d\omega - \dots \quad (12)$$

Comparing eq 12 with eq 10, the expression for the even moments of the VACF in terms of the normalized DOS are

$$\omega_v^{2n} = \int_0^\infty \Psi(\omega) \omega^{2n} d\omega \quad n = 1, 2, \dots \quad (13)$$

The parameters of the  $\gamma$  distribution (eq 7) are related to the frequency moments using eq 13. Since only the even moments (eq 13) are required while developing short time expansions for the VACF, the second and fourth frequency moments of the VACF, obtained by evaluating eq 13 for the  $\gamma$  distribution, are

$$\omega_v^2 = \frac{m(m+1)}{\alpha^2} \quad (14)$$

and

$$\omega_v^4 = \frac{m(m+1)(m+2)(m+3)}{\alpha^4} \quad (15)$$

Rearranging eqs 14 and 15 as a quadratic for  $m$ , the corresponding roots will be of different signs if  $[\omega_v^4 - (\omega_v^2)^2] > 0$ . This condition is satisfied for all the state points we have studied. The expression for the *positive* value of  $m$  in terms of  $\omega_v^2$  and  $\omega_v^4$  and the *positive* value of  $\alpha$  corresponding to this value of  $m$  are, respectively

$$m = \frac{[5(\omega_v^2)^2 - \omega_v^4] + \sqrt{[\omega_v^4 - 5(\omega_v^2)^2]^2 + 24(\omega_v^2)^2[\omega_v^4 - (\omega_v^2)^2]}}{2[\omega_v^4 - (\omega_v^2)^2]} \quad (16)$$

and

$$\alpha = \frac{\sqrt{4\omega_v^2[(\omega_v^2)^2 + \omega_v^4] + 2\omega_v^2\sqrt{[\omega_v^4 - 5(\omega_v^2)^2]^2 + 24(\omega_v^2)^2[\omega_v^4 - (\omega_v^2)^2]}}}{[\omega_v^4 - (\omega_v^2)^2]} \quad (17)$$

Equations 16 and 17 provide the relations that relate the parameters of the distribution to the frequency moments. The

above method for determining the parameters of the  $\gamma$  model ensures that the resulting DOS is accurate up to the fourth frequency moment. The frequency moments take a central place in theories concerned with the dynamics of the liquid state. For a bulk liquid, the frequency moments can be obtained directly from the pair-correlation function or static structure factor. More generally, the frequency moments can be computed directly from particle velocities generated during an MD simulation by using eq 11.

**2.4. Frequency Moments.** From eq 11, the moments can be directly obtained from the particle velocities<sup>19,20</sup> generated during the MD simulation. The second moment is computed using

$$\omega_v^2 = \frac{\langle \dot{v}_x(0)^2 + \dot{v}_y(0)^2 + \dot{v}_z(0)^2 \rangle_{t,N}}{\langle v_x(0)^2 + v_y(0)^2 + v_z(0)^2 \rangle_{t,N}} \quad (18)$$

where  $v_x$ ,  $v_y$ , and  $v_z$  are the single particle velocities in Cartesian coordinates and  $\langle \dots \rangle_{t,N}$  denotes time as well as particle averages. The fourth moment

$$\omega_v^4 = \frac{\langle \ddot{v}_x(0)^2 + \ddot{v}_y(0)^2 + \ddot{v}_z(0)^2 \rangle_{t,N}}{\langle v_x(0)^2 + v_y(0)^2 + v_z(0)^2 \rangle_{t,N}} \quad (19)$$

Derivatives of the velocities were computed numerically at every time step using a first-order finite difference scheme.

**2.5. Relaxation Time.** We use the relaxation time from  $\Psi(t)$  as a suitable measure of the ability of the model to capture the short time dynamics of the system. The relaxation time is sometimes used as a parameter while developing models for the VACF.<sup>19</sup> A convenient definition of  $\tau$ , the relaxation time, is<sup>21,22</sup>

$$\tau = 2 \int_0^\infty [\Psi(t)]^2 dt \quad (20)$$

Substituting the analytical expression for the VACF (eq 9) into eq 20, we obtain an analytical expression for the relaxation time in terms of the parameters of the model

$$\tau_\gamma = \frac{\sqrt{\pi}}{2} \alpha \frac{\Gamma(m - \frac{1}{2})}{\Gamma(m)} \quad (21)$$

### 3. Bulk Fluid

In this section, followed by the simulation details, we present results for the DOS, VACFs, and relaxation times for a bulk liquid.

**3.1. Bulk Fluid: Simulation Details.** Microcanonical (NVE) MD simulations for bulk fluids were carried out for 256 particles. All results are reported in reduced units as shown in Table 1. The fluid–fluid interactions are assumed to be a Lennard-Jones (LJ) 12-6 potential

$$u(r_{ij}) = 4\epsilon_{ff} \left[ \left( \frac{\sigma_{ff}}{r_{ij}} \right)^{12} - \left( \frac{\sigma_{ff}}{r_{ij}} \right)^6 \right] \quad (22)$$

where  $\epsilon_{ff}$  and  $\sigma_{ff}$  are the LJ potential parameters. Bulk fluid simulations have been carried out for liquid-state points given in Tables 2 and 3. The system was equilibrated for 50 000 time steps, each time step corresponding to  $\Delta t^* = 0.004$ . Simulations were conducted for an additional 50 000 time steps after equilibration during which 400 equally spaced configurations were used to calculate the INM DOS. At any instantaneous

**TABLE 1: Reduced Units Used in This Work**

quantity	reduced unit
slit width	$H^* = H/\sigma_{ff}^a$
box length	$L^* = L/\sigma_{ff}$
time	$t^* = t\sqrt{\epsilon_{ff}/Mo_{ff}^2}$
temperature	$T^* = kT/\epsilon_{ff}^a$
density	$\rho^* = \rho\sigma_{ff}^3$
velocity	$v^* = v\sqrt{M/\epsilon_{ff}}$
force	$F^* = F\sigma_{ff}/\epsilon_{ff}$
frequency	$\omega^* = \omega\sqrt{Mo_{ff}^2/\epsilon_{ff}}$
self-diffusivity	$D^* = D\sqrt{M/\epsilon_{ff}\sigma_{ff}^2}$

<sup>a</sup>  $\epsilon_{ff}$  and  $\sigma_{ff}$  are the Lennard-Jones parameters for the fluid–fluid interactions.

**TABLE 2: Values for the Second Moment of VACF,  $\omega_v^{*2}$  and Fourth Moment,  $\omega_v^{*4}$  for bulk fluid at different state points**

$\rho^*$	$T^*$	$(\omega_{v,INM}^2)^*{}^a$	$(\omega_{v,MD}^2)^*{}^b$	$(\omega_{v,INM}^4)^*{}^a$	$(\omega_{v,MD}^4)^*{}^b$	$m$	$\alpha^*$
0.83	1.03	314	313	339985	335464	1.93	0.134
0.83	3.03	565	565	1448721	1448656	1.36	0.075
0.83	0.79	273	272	240209	237379	2.10	0.154

<sup>a</sup>  $(\omega_{v,INM}^2)^*$  and  $(\omega_{v,INM}^4)^*$  correspond to values of the second and fourth frequency moments calculated from both the *real* and *imaginary* lobes of the DOS. <sup>b</sup>  $(\omega_{v,MD}^2)^*$  (eq 18)  $(\omega_{v,MD}^4)^*$  (eq 19) are the MD results. For all the state points studied, the computed moments from the INM DOS are in good agreement with the MD results.

**TABLE 3: Frequency Moments and Parameters of the  $\gamma$  Model,  $m$ , and  $\alpha$  for the Bulk Fluid**

$\rho^*$	$T^*$	$(\omega_v^2)^*$	$(\omega_v^4)^*$	$m^a$	$\alpha^*$	$\tau_\gamma^b$	$\tau_{MD}^b$	$(m-1)^{c/}$	$\omega_{max}^*$
1.0	1.28	597	949224	2.73	0.130	0.080	0.074	13.3	13.26
0.83	0.48	216	133300	2.47	0.199	0.132	0.122	7.38	7.37
0.83	0.79	272	237379	2.10	0.155	0.116	0.108	7.09	7.90
0.83	1.0	308	322547	1.96	0.137	0.108	0.100	7.00	7.85
0.83	1.51	382	550308	1.71	0.110	0.098	0.092	6.45	
0.83	2.91	550	1360118	1.38	0.077	0.082	0.078	4.94	
0.78	0.50	187	112055	2.13	0.188	0.140	0.130	6.01	5.80
0.78	1.48	325	438186	1.52	0.108	0.116	0.100	4.80	
0.78	3.02	488	1195328	1.22	0.074	0.090	0.086	2.97	

<sup>a</sup>  $m$  increases with density and decreases with an increase in temperature at constant density. <sup>b</sup>  $\tau_\gamma$  values are higher than  $\tau_{MD}$  with the errors typically between 4 and 9%. <sup>c</sup> The maximum frequency predicted by the  $\gamma$  model  $[(m-1)/\alpha]$  is compared with those obtained from the DOS ( $\omega_{max}$ ). For systems at high temperatures ( $T^* > 1.25$ ),  $\omega_{max}$  occurs at  $\omega = 0$  and is hence not reported.

configuration generated during the MD simulation, the eigenvalues of Hessian are obtained. The square roots of the eigenvalues give the characteristic frequencies of the system. The normalized DOS is the distribution obtained by binning these frequencies and taking an average over a number of different configurations.

It has been shown that the INM theory predicts the moments of the VACF exactly up to the fourth moment provided both the lobes of INM DOS are used.<sup>8–10,23</sup> In Table 2, we have compared the values of the second and fourth frequency moments obtained using both lobes of the INM DOS, with the moments obtained from the MD simulations using particle velocities (eqs 18 and 19). Consistent with the theory, the second and fourth frequency moments from the INM DOS are in good agreement with the MD results.

**3.2. Bulk Fluid: Predictions of the  $\gamma$  Model.** In this section, we apply the model for the DOS based on  $\gamma$  distributions. The  $\gamma$  distribution is constructed to retain the accuracy of the second and fourth moments. As a consequence, the predictions of the



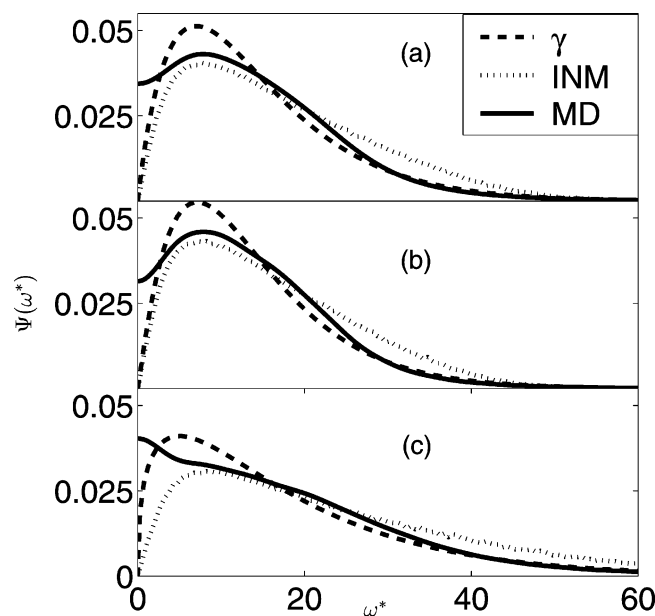


**Figure 2.** Comparison of INM DOS with the  $\gamma$  model prediction and molecular dynamics results for bulk liquids: (a)  $\rho^* = 0.83$  and  $T^* = 1.034$ , (b)  $\rho^* = 0.83$  and  $T^* = 0.788$ , and (c)  $\rho^* = 0.83$  and  $T^* = 3.033$ . The  $\gamma$  model and INM predict the dominant frequency in the liquid. Although the INM DOS is more accurate in the vicinity of the maximum frequency, the predictions of the  $\gamma$  model are more accurate at higher frequencies.

DOS and corresponding VACF based on the  $\gamma$  model are expected to be of greater accuracy than the conventional approach based on the real lobe of the INM DOS. The two parameters of the  $\gamma$  model  $m$  and  $\alpha$  are obtained from  $\omega_v^2$  and  $\omega_v^4$  using eqs 16 and 17. MD simulations were carried out over a range of temperatures for two different densities  $\rho^* = 0.83$  and  $0.78$  (Table 3). The  $\gamma$  distribution thus obtained is compared with the real lobe of the INM DOS in Figure 2 for a few selected state points (Table 2). We also report the DOS of the system obtained as the Fourier transform of the VACF in Figure 2.

Unlike the INM DOS which has a zero y-intercept, the DOS obtained from the VACF has a nonzero intercept, whose magnitude is proportional to the self-diffusivity of the system. The DOS from the  $\gamma$  model and the INM both predict a zero self-diffusivity. At lower temperatures (parts a and b of Figure 2), the INM DOS is able to accurately predict the distinct maxima which appears at lower frequencies. The  $\gamma$  model predicts the position of the maxima quite accurately, however, the corresponding DOS has a larger magnitude around the maxima. The frequency at which the maximum occurs in the  $\gamma$  model, which is  $(m - 1)/\alpha$ , is compared with the frequency obtained from the DOS (Table 3). An increase in temperature shifts the location of the maxima in the  $\gamma$  distribution to lower frequencies as the system becomes more fluidlike. This trend is reflected in Table 3. At higher frequencies, the  $\gamma$  model provides an excellent representation to the DOS. The improved performance of the  $\gamma$  model over the INM DOS at higher frequencies is due to the built in accuracy of the  $\gamma$  model up to the fourth frequency moment. We note that the frequency moments obtained only from the real lobe of the INM DOS are larger than the actual moments of the system.<sup>18</sup> This results in an increase in the contribution to the DOS (Figure 2) at higher frequencies from the INM DOS.

VACF predictions of the model based on the  $\gamma$  distribution,  $\text{VACF}_\gamma$ , are compared against the VACF obtained from the real lobe of INM DOS ( $\text{VACF}_{\text{INM}}$ ) and the VACF obtained from MD simulations ( $\text{VACF}_{\text{MD}}$ ). The results for the VACFs are

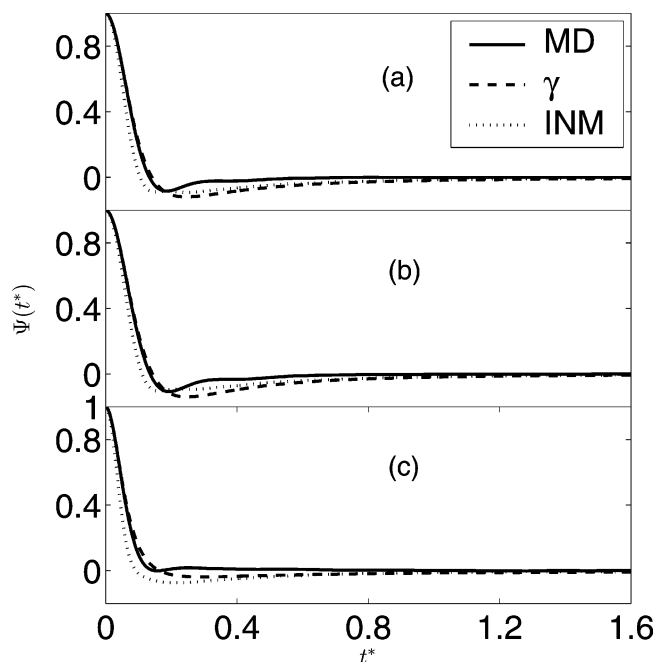


**Figure 3.** Comparison of the  $\gamma$  model prediction of the VACF with the VACF from INM and MD simulations. The corresponding DOS are shown in Figure 2: (a)  $\rho^* = 0.83$  and  $T^* = 1.034$ , (b)  $\rho^* = 0.83$  and  $T^* = 0.788$ , and (c)  $\rho^* = 0.83$  and  $T^* = 3.033$ . In all cases, the predictions of the  $\gamma$  model at short times are superior to the predictions from the INM theory. The VACF predicted from the INM (real lobe) is seen to relax faster than the VACF obtained from MD simulations.

shown in Figure 3. The corresponding DOS are shown in Figure 2. In all three cases,  $\text{VACF}_\gamma$  is seen to accurately predict the VACF at short and intermediate times and in this regime is superior to the predictions of the INM DOS theory. At short times,  $\text{VACF}_{\text{INM}}$  is seen to relax faster when compared with  $\text{VACF}_{\text{MD}}$ . The accuracy of the moments in the  $\gamma$  model is reflected in the superior prediction by  $\text{VACF}_\gamma$  in this regime. Around the region of the minima in the VACF, the  $\gamma$  model has a sustained region of negative correlations. Since the  $\gamma$  model predicts a zero diffusivity by construction, the negative correlations compensate for the accurate predictions of the VACF at short times where the VACF is positive. The  $\text{VACF}_\gamma$  compared with  $\text{VACF}_{\text{MD}}$  for the other state points investigated is plotted in Figure 4. Since the trends in the VACF from the INM DOS are similar to those shown in Figure 3, we did not report the  $\text{VACF}_{\text{INM}}$  in Figure 4. The model performance and trends are qualitatively similar to the results in Figure 3. The  $\gamma$  model is very flexible and is seen to work over a wide range of temperatures as shown in Figure 4. The short time prediction is seen to be the most accurate at the highest density liquid-state point  $\rho^* = 1.0$ .

**3.3. Bulk Fluid: Relaxation Time.** Since models based on both the  $\gamma$  and INM DOS are only valid for short times, both models predict a zero diffusivity. As a measure of the accuracy of the short time predictions of the  $\gamma$  model, we computed the relaxation times (eq 21) and compared them with  $\tau_{\text{MD}}$  values obtained by numerically integrating eq 20 with  $\text{VACF}_{\text{MD}}$ . The relaxation times are compared in Figure 5a and Table 3. The results shown in Figure 5a illustrate that the model is able to accurately capture the changes in the relaxation time with density and temperature. Although  $\tau_\gamma$  is quite accurate, it is slightly higher than  $\tau_{\text{MD}}$ . For the data points investigated, the largest errors in the relaxation time predictions were found to be less than 9% and the smallest errors were about 4%. The errors are lower for the lower density state points,  $\rho^* = 0.78$ , and decrease

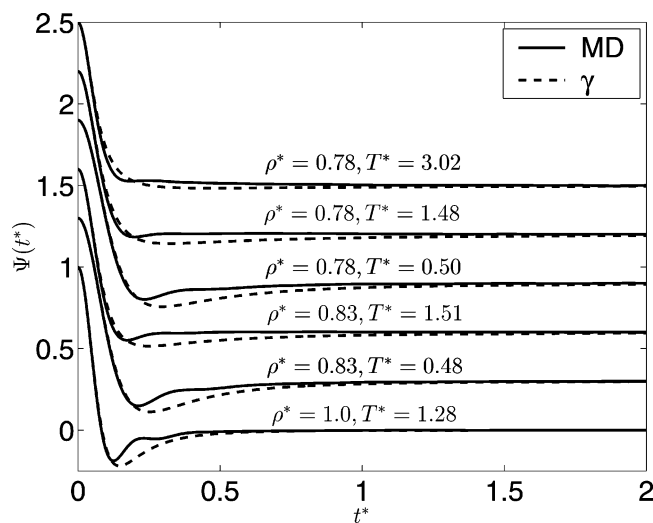


**Figure 4.** Comparisons for VACF predicted by the  $\gamma$  model with MD results. Except for the mismatch at intermediate times, the agreement is quite accurate. The results for  $\rho^* = 1.0$  are particularly accurate.

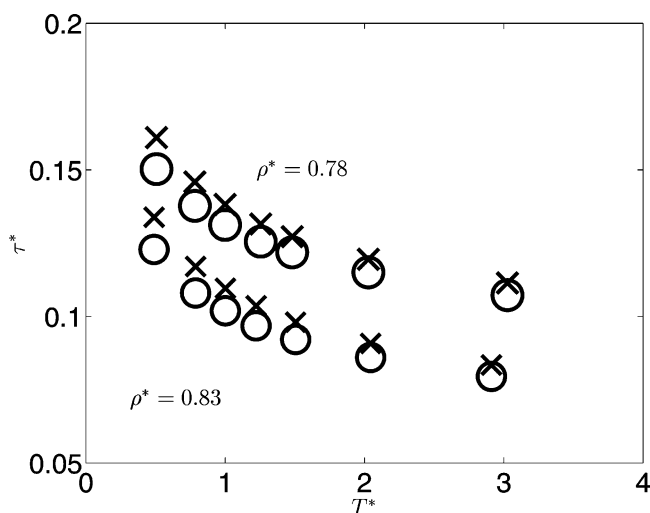


**Figure 5.** Comparisons for the relaxation time  $\tau$  for state points given in Table 3. The values for  $\rho^* = 0.78$  have been shifted by 0.02 units along the y-axis. At both densities, the predictions improve with increasing temperature. The model accurately predicts the decreasing relaxation time as the temperature is increased.

as the temperature is increased. The reason for this lies in the nature of the VACFs at these temperatures (Figure 4). At lower densities and higher temperatures, the improved agreement between  $VACF_{MD}$  and  $VACF_{\gamma}$  is reflected in the smaller errors in the relaxation times. The increased error in the relaxation time at lower temperatures is mainly due to the increased negative correlations typically observed in the predictions of the VACF by the  $\gamma$  model (Figure 4).

**3.4. Bulk Fluid: Parameters of the  $\gamma$  Model.** In this section, we discuss the trends observed in the parameters  $m$  and  $\alpha$  of the  $\gamma$  distribution as a function of temperature. This exercise was carried out to investigate whether the parameters of the  $\gamma$  distribution possess any useful scalings with temperature. Table 3 illustrates the values of the parameters for two different liquid densities over a range of temperatures. We note that  $m$  in the  $\gamma$  distribution determines the initial rise in the DOS and  $\alpha$  which determines the decay can be interpreted as a characteristic time in the system. The relaxation time based on the interpretation given in eq 20 yields an expression where  $\alpha$  is directly proportional to  $\tau$ . Figure 6 illustrates the temperature dependence of the parameters  $m$  and  $\alpha$  for both densities investigated. The

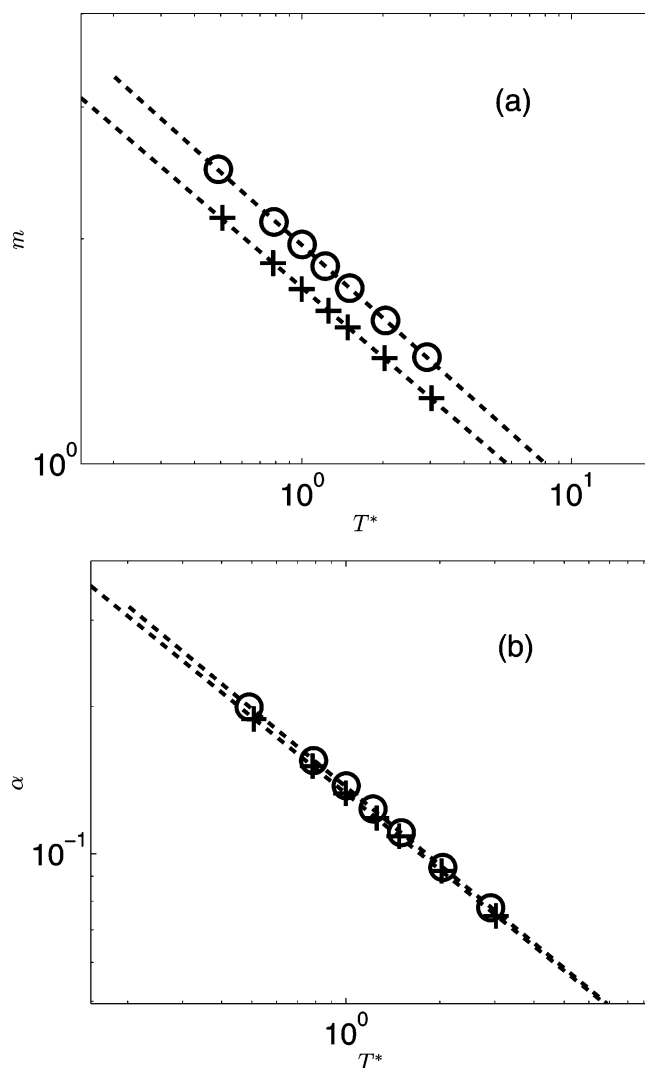


**Figure 6.** Temperature dependence of (a) parameter  $m$  and (b) parameter  $\alpha$  of the  $\gamma$  model: (O)  $\rho^* = 0.83$ , (+)  $\rho^* = 0.78$ . The dashed lines are the power law fit of the form  $a/T^{*b}$ . The parameters of the fit are given in Table 4. The power law is seen to provide an excellent representation to the temperature dependence of the parameters.  $T^*$  at which  $m = 1$  is 5.75 at  $\rho^* = 0.78$  and  $T^* = 7.87$  for  $\rho^* = 0.83$ .  $m = 1$  provides a lower bound on the applicability of the  $\gamma$  model.

**TABLE 4: Parameters for the Power Law Fits<sup>a</sup> for  $m = a/T^{*b}$  and  $\alpha = a/T^{*b}$**

	$\rho^*$	$a$	$b$
$m$	0.78	1.721	0.3094
$\alpha^*$	0.78	0.1329	0.5183
$m$	0.83	1.961	0.3235
$\alpha^*$	0.83	0.137	0.5295

<sup>a</sup> The accuracy of the fits is shown in Figure 6.

linear dependence on temperature of both parameters when plotted on a log–log scale suggest a  $1/T^b$  (algebraic scaling) dependence of both parameters with the temperature. In Table 4, we report the values for the power law fit of the form

$$m = \frac{a}{T^{*b}} \quad (23)$$

where  $a$  and  $b$  are positive constants. A similar functional form is used for  $\alpha$ . The value of the power law exponent  $b$  is relatively insensitive to the density of the fluid (in the temperature range investigated) for both  $m$  and  $\alpha$  (Table 4). In the case of  $\alpha$ , both

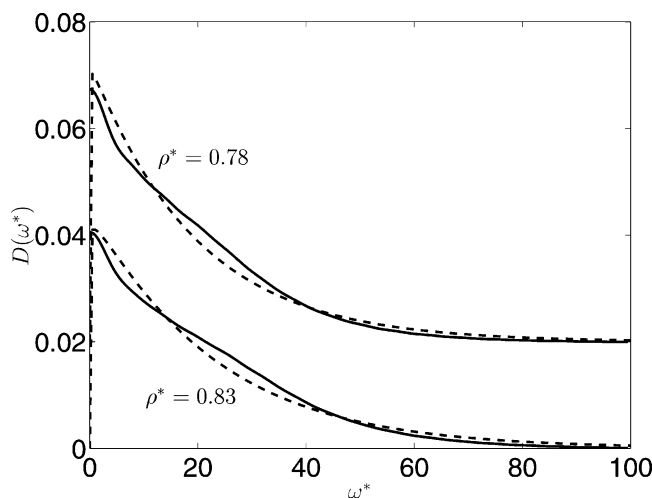


**Figure 7.** Comparisons of the DOS predicted by the  $\gamma$  model (dashed lines) at  $T^* = 5.75$ ,  $\rho^* = 0.78$  and  $T^* = 7.87$ ,  $\rho^* = 0.83$  (shifted by 0.02 y-axis units). At these state points, the parameters obtained from the simulations are  $m = 1.014$  and  $1.034$  and  $\alpha = 0.0529$  and  $0.0459$  for  $\rho^* = 0.78$  and  $\rho^* = 0.83$ , respectively. Interestingly, the intensity in the maxima of the  $\gamma$  model which occurs at lower frequencies coincides with the  $\gamma$ -intercept (diffusive limit) of the DOS.

parameters of the power law are found to be insensitive to the fluid density. The accurate representation of the model parameters using the power law fit suggests that expressions of the form given in eq 23 can be used to obtain the DOS from the  $\gamma$  model for other temperatures at the two fluid densities investigated. Further, since the parameters of eq 23 are obtained using reduced units, the scalings are expected to be universally applicable to any Lennard-Jones fluid. Since the  $\gamma$  model is valid for  $m > 1$ , the power law scaling of the parameter  $m$  suggests that the temperature at which  $m = 1$ , which provides an upper bound on the validity of the model, can be obtained from Figure 6a. The corresponding temperatures are  $T^* = 5.75$  at  $\rho^* = 0.78$  and  $T^* = 7.87$  at  $\rho^* = 0.83$ . To confirm the predicted scalings, MD simulations at  $T^* = 5.75$  at  $\rho^* = 0.78$  result in  $m = 1.014$  and  $\alpha = 0.0529$ . At  $T^* = 7.87$  at  $\rho^* = 0.83$ , we obtain  $m = 1.034$  and  $\alpha = 0.0459$ . Both the values of  $m$  obtained from the MD simulations being close to unity are consistent with the predictions of eq 23. The comparisons of the  $\gamma$  model with the DOS at these conditions are illustrated in Figure 7. As  $m$  approaches unity, the  $\gamma$  model reduces to an exponential distribution as illustrated. More importantly, our results clearly indicate that the  $\gamma$  model is able to adapt to the changes in the DOS of the fluid as the temperature is varied over a wide range. Interestingly, the intensity of the most populated frequency, which is close to  $\omega = 0$ , matches with the value of the self-diffusivity of the system.

#### 4. Spherical Cavity

The predictions of the  $\gamma$  model are developed on short time expansions of the VACF, and the INM DOS analysis is based on a harmonic approximation. By construction, these models are not designed to predict the long time diffusive behavior.  $\text{VACF}_\gamma$  and  $\text{VACF}_{\text{DOS}}$  are models which both predict a zero self-diffusivity. Hence, both the real lobe INM DOS and the  $\gamma$  DOS have a zero intercept at  $\omega = 0$ . In this section, we investigate the dynamics of molecules confined to a spherical cavity. The primary motivation for examining this system is to test the applicability of the INM analysis and the  $\gamma$  based model for a system of particles which is inherently zero diffusive.

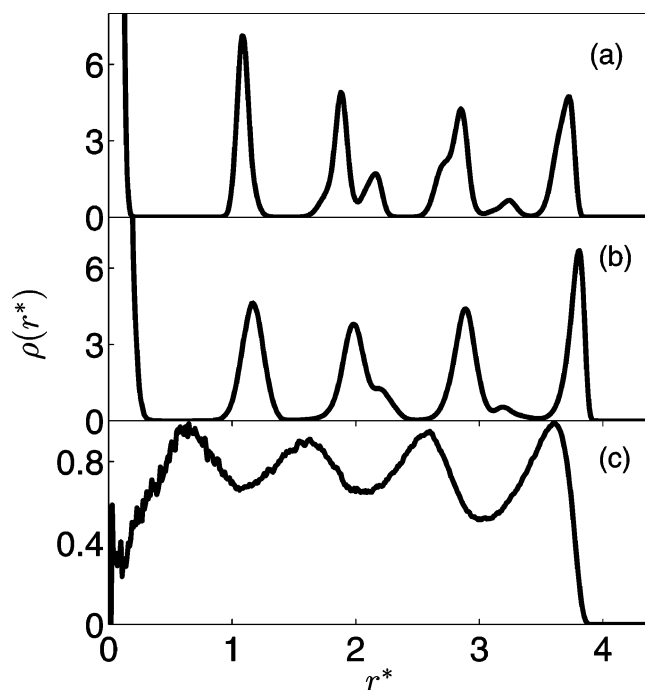


**Figure 8.** Density distributions within the spherical cavity: (a)  $N = 300$ ,  $T^* = 0.38$ , (b)  $N = 360$ ,  $T^* = 1.22$ , and (c)  $N = 170$ ,  $T^* = 1.26$ . At higher loadings (a) and (b) the fluid is organized into well-defined concentric shells.

**4.1. Spherical Cavity: Simulation Details.** We consider spherical molecules interacting with a LJ potential ( $\sigma = 3.405$  Å,  $\epsilon/k_B = 120$  K) confined in a spherical cavity of radius  $4.44\sigma$ . The interaction potential for the fluid confined in a spherical cavity is similar to the potential used to describe the interaction of a molecule in the interior of a reverse micelle with the hydrocarbon chains that make up the walls of the reverse micelle.<sup>24,25</sup> The interaction of the fluid molecules with the cavity has the following form

$$U_{fc}(z) = 8\pi\rho_c\epsilon\sigma^3[(\sigma/R)^9F_6(z) - (\sigma/R)^3F_3(z)] \quad (24)$$

where

$$F_3(z) = \frac{2}{[3(1 - z^2)^3]} \quad (25)$$

and

$$F_6(z) = \frac{2(5 + 45z^2 + 63z^4 + 15z^6)}{[45(1 - z^2)^9]} \quad (26)$$

In the above equations, the reduced distance,  $z = r/R$ , where  $r$  is the radial distance of the particle from the center of the cavity and  $\rho_c\sigma^3 = 0.1414$ . The energy parameter in eq 24 is similar to the value used for the fluid–fluid interaction. As an added check on the accuracy of the computed moments, the moments obtained from the INM DOS are compared with the moments obtained from the MD simulations. Both  $\omega_v^2$  and  $\omega_v^4$  were found to be in good agreement.

**4.2. Spherical Cavity: Results and Discussion.** The density distributions for the fluid molecules inside a spherical cavity are shown in Figure 8. At the higher densities investigated (parts a and b of Figure 8), the fluid is seen to organize in spherical shells within the cavity, separated radially by about  $1\sigma$ . At the lowest density and highest temperatures, the density distribution (Figure 8c) indicates a more diffuse configuration. The corre-

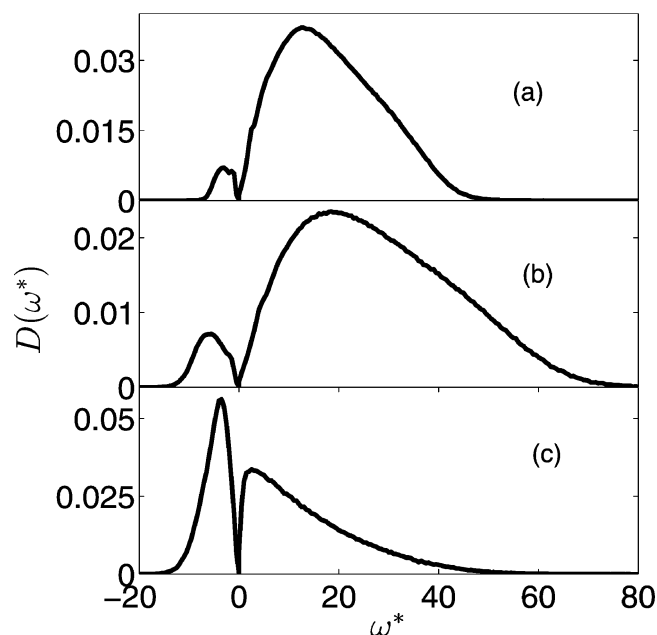


**Figure 9.** INM DOS for the spherical cavity: (a)  $N = 300$ ,  $T^* = 0.38$ , (b)  $N = 360$ ,  $T^* = 1.22$ , and (c)  $N = 170$ ,  $T^* = 1.26$ . At the higher densities, the contributions to the INM DOS from the imaginary lobe are significantly reduced.

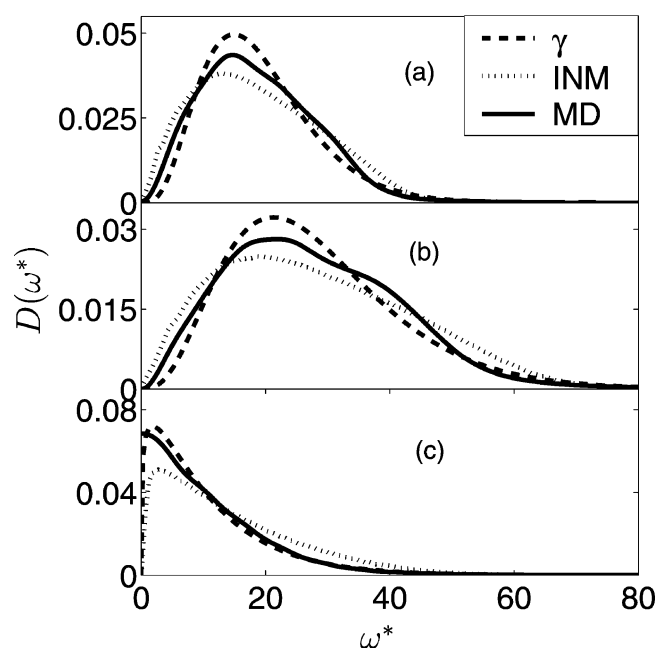


**Figure 10.** Spherical cavity INM DOS compared with the DOS and the  $\gamma$  model: (a)  $N = 300$ ,  $T^* = 0.38$ , (b)  $N = 360$ ,  $T^* = 1.22$ , and (c)  $N = 170$ ,  $T^* = 1.26$ . The zero-diffusive nature of the system is reflected in the zero intercept of the DOS obtained from the MD simulations. Similar to the trends observed for bulk liquids, the  $\gamma$  model is more accurate at higher frequencies. In the low-density situation (a), the  $\gamma$  model is very accurate.

sponding INM DOS are illustrated in Figure 9. At higher densities, the intensity of the imaginary lobe of the INM DOS is seen to decrease significantly (parts a and b of Figure 8). In these situations, the DOS is dominated by the contribution from the real lobe of the DOS. At higher temperatures, however, the contributions from the imaginary lobes are quite significant and the real lobe resembles an exponentially decaying function (Figure 8c). Figure 10 compares the DOS obtained from the MD simulations and  $\gamma$  model with that of the INM DOS, since the fluid confined in a spherical cavity does not possess a long

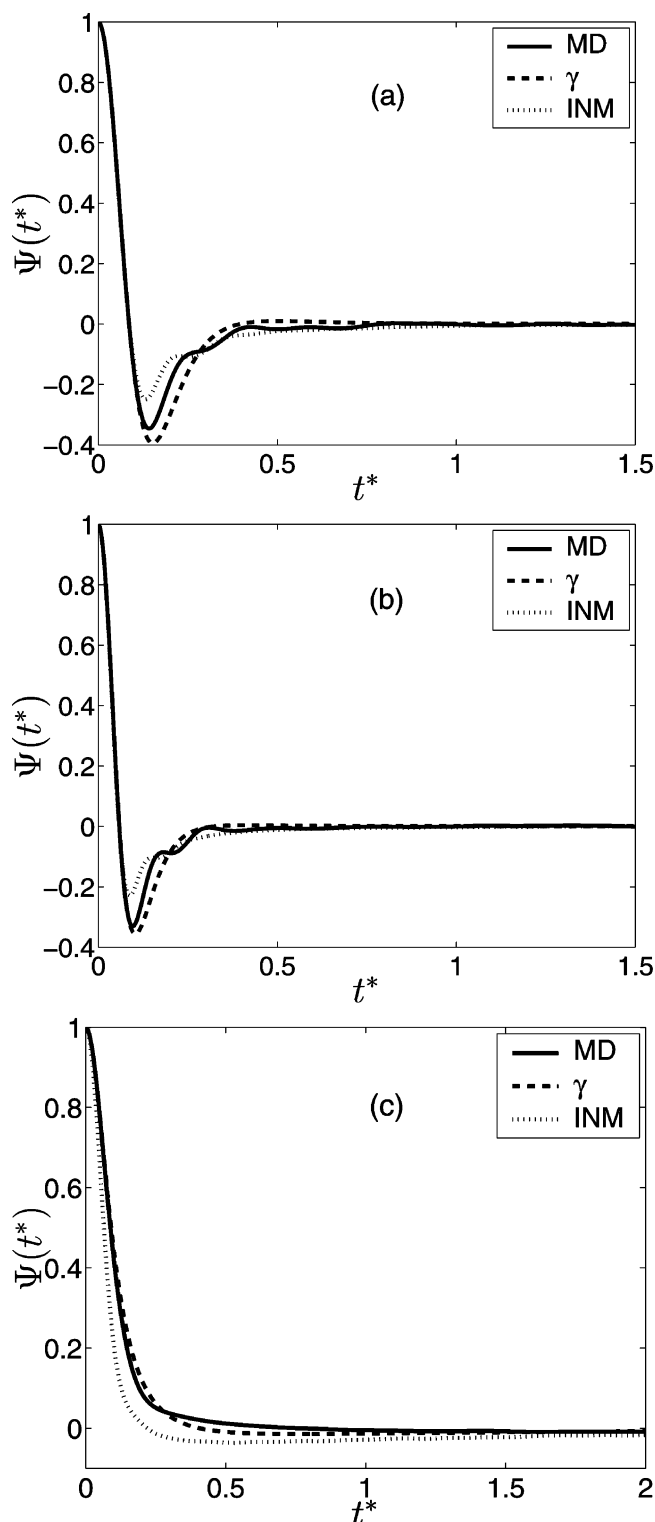


**Figure 11.** Comparison of VACFs predicted by the  $\gamma$  model for spherical cavity: (a)  $N = 300$ ,  $T^* = 0.38$ , (b)  $N = 360$ ,  $T^* = 1.22$ , and (c)  $N = 170$ ,  $T^* = 1.26$ . For lower densities, the  $\text{VACF}_{\text{INM}}$  is unable to give accurate predictions. However, the predictions from both the  $\gamma$  model and INM theory are similar at short times. The improved predictions by the INM theory at the higher density are due to the smaller contributions from the imaginary lobe to the overall DOS as seen in Figures 9a and 9b.

time diffusivity,  $\Psi(\omega^* = 0) = 0$ , for the DOS obtained from the MD simulations. This situation is appropriate for modeling the dynamics using the INM DOS and  $\gamma$  models which are inherently nondiffusive in nature and developed mainly to



**TABLE 5: Frequency Moments and Values of Model Parameters  $m$  and  $\alpha$  with Predicted Values of  $\tau_\gamma$  for the Spherical Cavity Compared with  $\tau_{MD}$** 

$N$	$\rho^*$	$T^*$	$(\omega_v^2)^*$	$(\omega_v^4)^*$	$m$	$\alpha^*$	$\tau_\gamma^*$	$\tau_{MD}^*$	$\frac{\tau_\gamma^* - \tau_{MD}^*}{\tau_{MD}^*} \times 100$
147	0.40	0.38	343	379262	2.09	0.137	0.104	0.099	4.2323
256	0.69	1.20	311	549669	1.065	0.084	0.121	0.113	6.8755
256	0.69	0.48	325	364724	1.91	0.131	0.106	0.099	6.8460
312	0.85	1.23	424	759075	1.490	0.093	0.094	0.088	5.9405
312	0.85	0.40	323	316574	2.28	0.152	0.108	0.101	6.1286
349	0.95	1.16	526	957164	1.913	0.102	0.083	0.078	6.3648
349	0.95	0.39	346	334719	2.55	0.161	0.106	0.100	5.5148
439	1.19	1.20	1038	2538003	3.299	0.117	0.064	0.060	6.8141
439	1.19	0.39	828	1316284	4.73	0.181	0.080	0.070	14.2935
451	1.23	1.19	1131	2906783	3.502	0.118	0.062	0.059	6.4003
451	1.23	0.39	945	1669762	5.00	0.178	0.076	0.066	14.2351

explore the short time dynamics of the fluid. The qualitative features of DOS predicted by the  $\gamma$  model and the INM DOS are similar to those observed in bulk fluids. The higher values of the INM DOS at higher frequencies are due to the larger positive deviations of the lower frequency moments, which arise from neglecting the contributions from the imaginary lobes. However, the agreement at higher frequencies is better for the  $\gamma$  model. Similar to the trends observed in slit-shaped pores,<sup>14</sup> the  $\gamma$  model is seen to provide a better match to the dominant resonant frequency in the system. Interestingly, the  $\gamma$  model is able to accurately capture the DOS for the gaslike situation as well (Figure 10c).

The predictions of the VACF for the corresponding situations shown in Figure 10 are illustrated in Figure 11. The best predictions with the  $VACF_{MD}$  are obtained by the  $\gamma$  model ( $VACF_\gamma$ ) for both the high-density (parts a and b of Figure 11) and low-density situations (Figure 11c). For the high-density situations, the deviations of  $VACF_{INM}$  are smaller than those observed for the bulk liquid results reported earlier in the paper and slit pore results.<sup>14</sup> This is due to the smaller contributions from the imaginary lobe of the INM DOS at higher densities and lower temperatures (Figure 9). For the high-density situations, the contributions to the second moment from the imaginary lobe to the overall INM DOS were found to be less than 0.2% and the contribution to the fourth moment was only 0.002%. As a result, the  $VACF_{INM}$  predicted from the real lobe alone retains sufficient accuracy, since the deviation from the actual frequency moments is less severe. The validity of the above argument is borne out in Figure 11c where the DOS has the largest contribution from the imaginary lobe (Figure 9c) and the deviation of  $VACF_{INM}$  is the greatest. In this case, the overall percentage contribution to the second moment from the imaginary lobe is 2.5% and from the fourth moment is 0.1%. Hence, the lowest density where the VACF is more like that of a gas (Figure 11c) the INM model performs poorly. In contrast, for a low-density system, the  $\gamma$  model is able to adapt to the monotonically decaying VACF (Figure 9c). At this density, the INM model is unable to predict any of the features of the VACF as the INM theory is expected to be less accurate at lower densities.

Relaxation times at both high and low temperatures for an increasing number of particles are plotted in Figure 12, and selected values are tabulated in Table 5. The  $\gamma$  model is able to predict the relaxation times for a range of densities at both high and low temperatures quite accurately. Particularly, the model is able to capture the trends in the relaxation time with an increase in loading and temperatures. The relaxation times (Figure 12b), at higher temperatures, are seen to monotonically decrease with temperature. However, at lower temperatures, the

relaxation time is relatively insensitive to loading for low and intermediate densities and decreases beyond a loading of  $N = 330$  particles in the cavity. Upon an increase in density, the particles tend to organize into layers. The enhanced layering of the fluid particles is reflected by a decrease in the relaxation time. From Table 5, it can be observed that the error in prediction of the relaxation time varies from a low value of

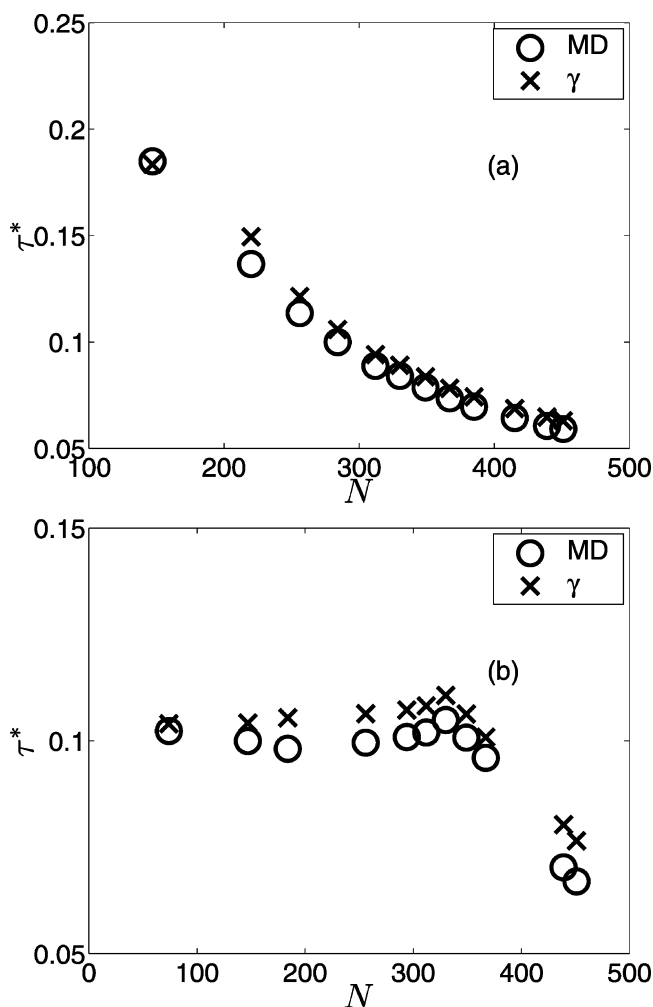


**Figure 12.** (a) Relaxation times predicted by the  $\gamma$  model for increasing number of particles in the spherical cavity: (a) high temperature and (b) low temperature. The numerical values and the ensemble averaged temperatures at selected points are given in Table 5. The predictions from the  $\gamma$  model accurately capture the changes in  $\tau$  due to density and temperature. The percentage deviation from the MD results are less than 7% for all the state points except the two highest density points where the error is about 14%.

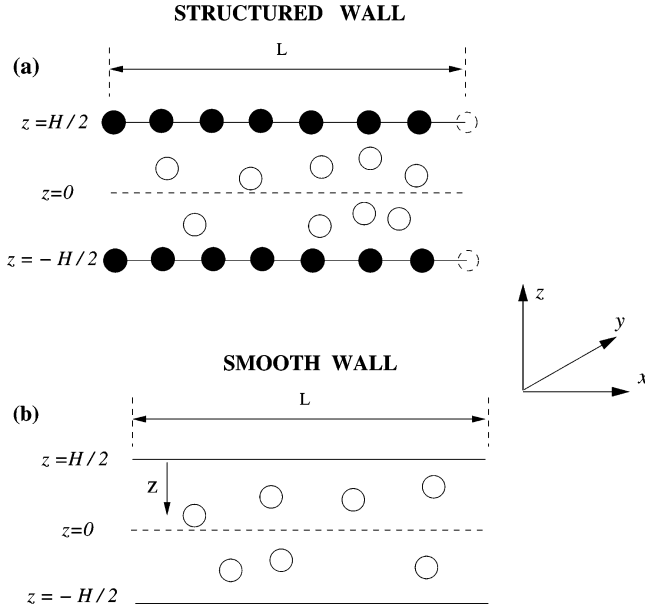


**Figure 13.** Schematic of (a) structured and (b) smooth slit pores indicating the pore width  $H$  and periodic box length  $L$ . Periodic boundary conditions are applied in the  $x$  and  $y$  directions.

less than 1% to as high as 9%, except at the highest densities and lower temperature (Table 5) where the error is around 14%.

## 5. Slit Pores

**5.1. Slit Pores: Simulation Details.** In this section, we obtain the relaxation time for a fluid confined in a slit-shaped pore. We consider results for both structured and smooth walled pores. Figure 13a illustrates a structured pore, of width  $H$  where the pore wall consists of discrete particles, and Figure 13b illustrates a smooth walled pore where the interaction of the wall with the fluid molecules is only in the  $z$  direction. The pores are infinite in the  $x$ - $y$  plane but finite in the  $z$  direction. For a confined fluid, the total potential energy is  $U = U_{ff} + U_{fw}$ , where  $U_{ff}$  is the total fluid–fluid interaction energy and  $U_{fw}$  is the total fluid–wall interaction. For a system with  $N$  fluid particles with pairwise additive potentials

$$U_{ff} = \sum_{i=1}^{N-1} \sum_{j>i}^N u(r_{ij}) \quad (27)$$

The fluid–fluid interactions are assumed to be 12-6 LJ interactions. For the structured pore, fluid–wall interactions are modeled using the 12-6 LJ potential with the potential parameters  $\epsilon_{fw}$  and  $\sigma_{fw}$ . The total fluid–wall potential for the structured pore consisting of  $N_w$  wall particles is

$$U_{fw} = \sum_{i=1}^N \sum_{j=1}^{N_w} u(r_{ij}) \quad (28)$$

The fluid–wall LJ interaction parameters used in this study are similar to the fluid–fluid interaction parameters. For the structured pore, each wall consisted of 200 particles arranged in a face centered cubic (fcc) lattice. This corresponds to a pore of side  $L^* = 14.14$ . For the smallest slit width of  $H^* = 2.0$ , we have used a larger simulation box of  $L^* = 20.5$  for better statistics.

For the smooth pore where the fluid–wall potential is only a function of the normal distance,  $z$ , of the fluid particle from

**TABLE 6: Model Parameters and Relaxation Times for the Structured Pores of Width  $H$**

$\langle N \rangle^a$	$H^*$	$T^*$	$(\omega_v^2)^*$	$(\omega_v^4)^*$	$m$	$\alpha^*$	$\tau_\gamma^*$	$\tau_{MD}^*$
139	2.15	1.19	227	225653	1.43	0.123	0.129	0.124
250	2.75	1.20	241	235102	1.56	0.129	0.124	0.122
269	3.25	1.27	216	231123	1.23	0.113	0.137	0.130
334	3.65	1.21	215	220768	1.30	0.117	0.135	0.129
366	3.85	1.17	214	215176	1.32	0.119	0.135	0.129
392	4.15	1.19	212	219040	1.27	0.116	0.136	0.130
408	4.35	1.20	208	213909	1.24	0.115	0.139	0.133
456	4.65	1.16	208	208266	1.28	0.118	0.137	0.132
492	4.9	1.21	215	223751	1.27	0.116	0.136	0.130
513	5.1	1.18	209	214193	1.26	0.116	0.138	0.132

<sup>a</sup> The ensemble averaged number of particles  $\langle N \rangle$  obtained from the GCMC simulations are also shown. The model predictions are very accurate although a small overestimation is observed. The errors in the predicted relaxation time range from 4 to 6%.

the wall, fluid–wall interactions were modeled using a 10-4 potential

$$u_{fw} = 2\pi\epsilon_{fw} \left[ \frac{2}{5} \left( \frac{\sigma_{fw}}{z} \right)^{10} - \left( \frac{\sigma_{fw}}{z} \right)^4 \right] \quad (29)$$

Equation 29 represents the interaction of the fluid particle with a single layer of atoms arranged in a fcc lattice. The total fluid–wall interaction in the smooth pore is the sum of the potential energies arising from two walls located at  $z_w = -H/2$  and  $z_w = H/2$ , respectively

$$U_{fw} = \sum_{i=1}^N u_{fw} \left( z_i + \frac{H}{2} \right) + u_{fw} \left( z_i - \frac{H}{2} \right) \quad (30)$$

where  $u_{fw}$  is given in eq 29 and  $z_i$  is the  $z$  coordinate of the  $i$ th fluid particle.

Since we are interested in the dynamics of fluids that are in equilibrium with a bulk fluid, we obtain the loadings in the slit pores at different heights from GCMC simulations. The details of the GCMC simulation procedures for confined fluids are standard and are given elsewhere.<sup>26,27</sup> The GCMC simulations correspond to a reduced bulk activity of  $Z^* = \exp(\beta\mu)/\Lambda^3 = 0.075114$  where  $\beta = 1/k_B T$  and  $\mu$  is the chemical potential of the bulk fluid.  $\Lambda = h/(2\pi M k_B T)^{1/2}$  is the thermal de Broglie wavelength where  $h$  is the Planck's constant and  $M$  is the mass of the particle. The simulations were carried out at a reduced temperature  $T^* = k_B T/\epsilon = 1.2$ . At this bulk fluid condition, the corresponding density is  $\rho^* = 0.661$  and the reduced pressure obtained from the 32 parameter equation of state<sup>28</sup> is 0.355. GCMC simulations were carried out for 15 million moves out of which 10 million moves were used for obtaining average quantities. In the case of the structured pore, each wall consisted of 168 particles arranged in a fcc lattice. This corresponds to a pore of side  $L_x = 13.81\sigma$  and  $L_y = 13.67\sigma$ . In the case of the smooth pore, GCMC simulations were carried out with a box of length  $7\sigma$ . In all cases, the GCMC simulations were started with an empty pore. The ensemble averaged number of particles obtained from the GCMC simulations for different pore widths are given in Tables 6 and 7 for the structured and smooth pores, respectively. Through the use of an ensemble averaged number of particles obtained from the GCMC simulations, molecular dynamics simulations were conducted in the NVE ensemble for 100 000 time steps, with 50 000 equilibration steps. For each step,  $\Delta t^* \approx 0.004 \approx 0.008$  ps. Simulations were carried out for slit widths which can accommodate one, two, three, and four layers inside the pore at  $T^* = 1.2$ . The time averaged equilibrium temperatures obtained from the molecular dynamics

**TABLE 7: Similar to Table 6 except for Smooth Pores**

$\langle N \rangle$	$H^*$	$T^*$	$(\omega_v^2)^*$	$(\omega_v^4)^*$	$m$	$\alpha^*$	$\tau_\gamma^*$	$\tau_{MD}^*$
152	2.25	1.20	250	277287	1.41	0.116	0.123	0.119
144	2.35	1.16	199	202368	1.20	0.115	0.144	0.138
164	2.5	1.16	224	236715	1.31	0.116	0.132	0.127
172	2.65	1.15	177	177876	1.06	0.111	0.161	0.152
252	2.75	1.24	245	276270	1.35	0.113	0.125	0.119
284	3.0	1.19	245	265860	1.41	0.117	0.124	0.118
292	3.2	1.16	237	249971	1.40	0.119	0.127	0.121
280	3.35	1.13	196	197012	1.19	0.115	0.145	0.140
312	3.5	1.21	222	238653	1.27	0.114	0.134	0.129
380	3.75	1.19	235	252578	1.36	0.117	0.127	0.122
412	4.0	1.16	232	244026	1.37	0.118	0.128	0.123
648	6.0	1.19	211	221972	1.23	0.114	0.138	0.133

simulations are also listed in the Tables 6 and 7. The frequency moments were computed using the in-plane  $x$  and  $y$  velocities of the particles only. Since the results of the VACF and density of states predictions from the INM analysis are similar to earlier studies on slit pores,<sup>14</sup> we focus only the predictions of the  $\gamma$  model in this paper.

**5.2. Slit Pore: Open Ensemble Results.** As the pore width is varied in a GCMC simulation, the pore fluid undergoes a series of layering transitions. Concomitant with these layering transitions are the oscillatory nature of the disjoining pressure and self-diffusivity at smaller pore widths. Hence, the diffusivity is seen to oscillate between well-ordered and disordered layers. These phenomenon are well documented in the confined fluids literature.<sup>26,27,29–31</sup> Since the relaxation time is a measure of the fluid mobility, it is expected to reflect the changes in the state of the pore fluid due to layering as the pore width is varied. The relaxation times (eq 20) for both smooth and structured pores obtained using the  $\gamma$  distribution are shown in Figures 15a and 14a, respectively. The plots also illustrate the corresponding self-diffusivities obtained from the MD simulations (Figures 15b and 14b). The numerical values for the relaxation times are tabulated in Tables 6 and 7. In both the structured and smooth pores, the  $\gamma$  model is able to capture the oscillations present in the relaxation time as the pore width is varied. Similar to the trends in the relaxation time obtained for the slit pore and bulk fluids in earlier sections,  $\tau_\gamma > \tau_{MD}$ . The oscillations in the relaxation time are similar to the oscillatory nature of the self-diffusivity in these systems, with the relaxation time increasing as the self-diffusivity of the confined fluid increases. The difference between the relaxation time between the  $\gamma$  model and the simulations range between 3.5 and 6%. In both cases, the oscillations in the relaxation time are very accurately captured. VACFs for the structured and smooth pores are illustrated in Figure 16. The trends in the predictions are similar to those observed earlier, with excellent agreement at short times and larger negative correlations at intermediate times. The larger negative correlations lead to a small overestimation in the relaxation times. However, given that the model is only accurate up to the fourth moment, the agreement with VACF<sub>MD</sub> is quite satisfactory.

## 6. Summary and Conclusions

In this paper, a recently proposed model for the density of states based on  $\gamma$  distributions<sup>14</sup> has been tested for a bulk liquid and for fluids confined in slit-shaped pores and spherical cavities. The performance of the model is evaluated by comparing the predicted relaxation times and VACFs with those obtained from molecular dynamics simulations and from INM analysis. Comparisons have been carried out for bulk fluids, fluids confined in structured and smooth walled pores, and fluids

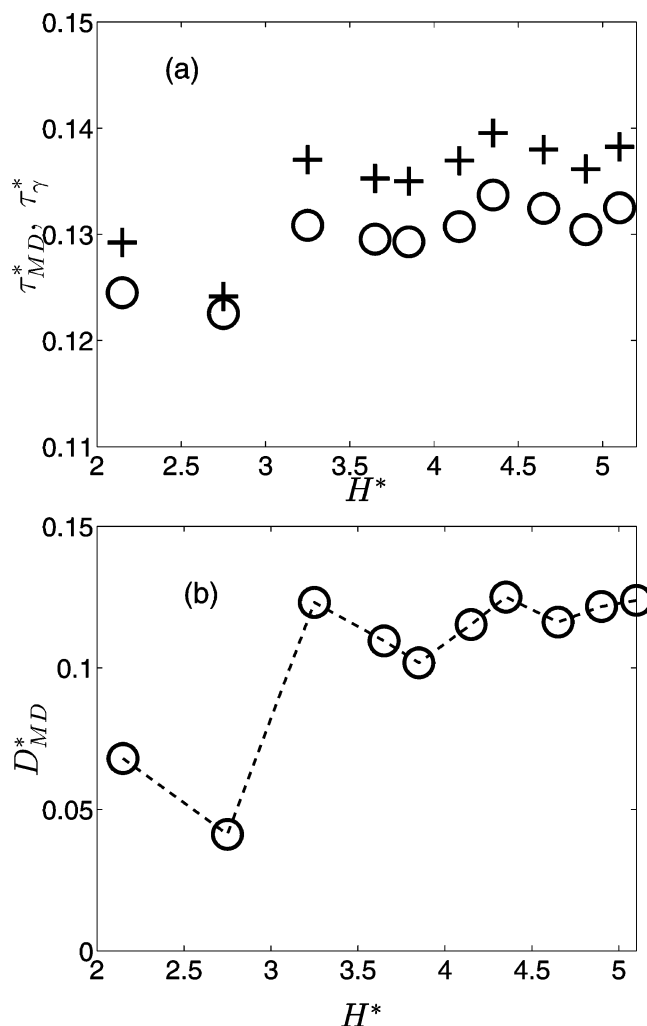


**Figure 14.** (a) Relaxation times for the structured pore for the GCMC state points. (O) are the MD results and (×) are the results of the model. (b) In-plane ( $x$ – $y$ ) self-diffusivities predicted from the MD simulations. The predicted relaxation times although slightly higher (<6% error) than the results obtained from simulations accurately capture the changes in relaxation time as the pore width  $H^*$  is increased. The oscillations in the relaxation time (a) due the formation and disruption of layers in the pore is reflected in the self-diffusivity data (b).

confined in a spherical cavity which is representative of a system which does not possess any long time diffusive behavior.

In the case of high-density bulk Lennard-Jones liquids, the predicted relaxation times from the  $\gamma$  model varied between 4 and 9% (higher) of the simulation values, with greater accuracy in the predictions at higher temperatures. The parameters of the  $\gamma$  distribution were found to scale with the inverse of the temperature at a fixed fluid density and can be used to accurately estimate the parameters at intermediate temperatures. In all cases, the built-in accuracy of the frequency moments in the  $\gamma$  model are reflected in the improved agreement of the VACFs over the INM predictions. In addition, the  $\gamma$  model is flexible and is seen to work over a wider range of thermodynamic conditions.

The spherical cavity results are reported over a wide range of densities and temperatures, and the resulting changes in the relaxation time are accurately captured by the  $\gamma$  model. In comparison to the slit pores, the smaller fraction of imaginary lobes present in the DOS for the spherical cavity improve the short time predictions of the VACF from the INM theory. Since the  $\gamma$  model and INM theory based on the real lobe of the DOS inherently predict a zero diffusivity by construction, the

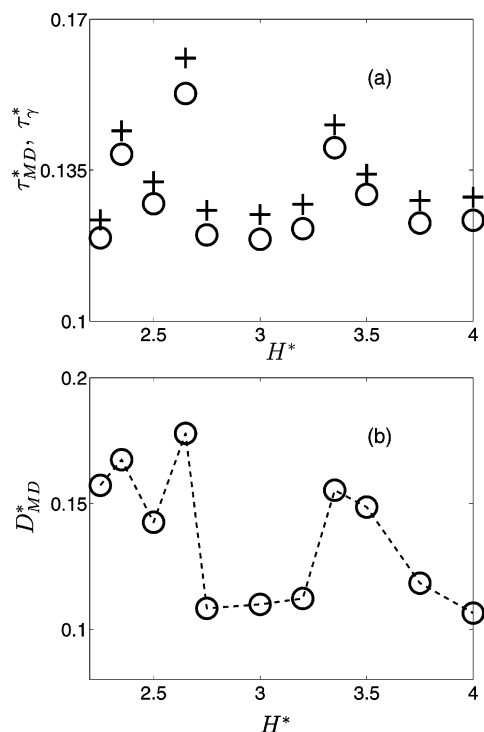


**Figure 15.** Same as Figure 14 but for the smooth walled pore.

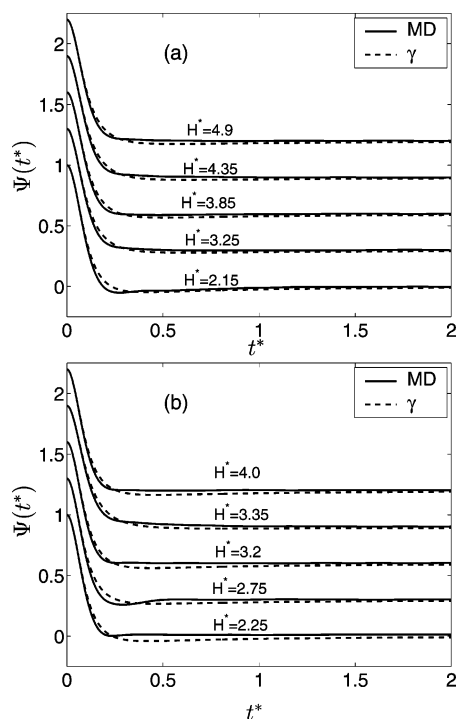


**Figure 16.** The  $\gamma$  model predictions of the VACFs for (a) structured and (b) smooth pores. Excellent agreement at short times and larger negative correlations at intermediate times are observed. These larger negative correlations lead to small positive deviations in the predicted relaxation times by the  $\gamma$  model (Figures 14a and 15a).

functional form of the approximation to the actual DOS in the spherical cavity is found to be more appropriate. Hence, predictions of the DOS, particularly at the lower and intermediate frequencies, and the corresponding short time prediction to the VACFs from both these models are superior to the predictions observed in the case of bulk liquids or fluids confined in slit pores. This suggests that both the  $\gamma$  and INM

models would be better suited for studying the short time dynamics and relaxation of strongly confined systems.

In the case of a fluid confined in a slit pore, we study the dynamics of the fluid as a function of the pore width. This system models the confinement situation in a surface force apparatus where a fluid is confined to a few molecular diameters. The pore densities are obtained from GCMC simulations where the pore is equilibrated with a bulk fluid at constant chemical potential and temperature. The relaxation time of the confined fluid oscillates with pore width, reflecting the structural changes due to the formation and disruption of fluid layers as the pore width is increased. The  $\gamma$  model is seen to accurately capture these variations in the relaxation time for both smooth and structured pores. Similar to the trends observed in bulk liquids and spherical cavities, the relaxation is within 6% of the simulated values.

Since the only inputs into the  $\gamma$  model are the frequency moments, the model presents a direct route to the short time dynamics and relaxation of bulk liquids, where the frequency moments can be obtained directly from the pair-correlation functions. The pair-correlation functions can be obtained from existing integral equation theories, Monte Carlo simulations, or directly from experimental structure factors. In the case of the confined fluids, however, we have obtained the frequency moments directly from velocities generated from the MD simulations. We point out that it is not necessary to carry out a MD simulation in order to obtain the second and fourth moments. These quantities can be obtained directly from a Monte Carlo simulation as well, by using the appropriate derivatives of the interatomic potentials.<sup>32</sup> Our study also illustrates that models for the VACF that are based on short time expansions can be used to extract a reliable measure of the relaxation time for strongly inhomogeneous fluids.

**Acknowledgment.** This work was carried out from support by the Center for High Technology (CHT), Ministry of Petroleum, India.

## References and Notes

- (1) Stillinger, F. H.; Weber, T. A. *Phys. Rev. A* **1982**, 25, 978.
- (2) Zwanzig, R. *J. Chem. Phys.* **1983**, 79, 4507.
- (3) Mohanty, U. *Phys. Rev. A* **1985**, 32, 3055.
- (4) Seeley, G.; Keyes, T. *J. Chem. Phys.* **1989**, 91, 5581.
- (5) Stratt, R. M. *Acc. Chem. Res.* **1995**, 28, 201.
- (6) Keyes, T. *J. Phys. Chem. A* **1997**, 101, 2921.
- (7) Antoniou, D.; Schwartz, S. D. *J. Chem. Phys.* **2001**, 115, 4670.
- (8) Buchner, M.; Ladanyi, B. M.; Stratt, R. M. *J. Chem. Phys.* **1992**, 97, 8522.
- (9) Adams, J. E.; Stratt, R. M. *J. Chem. Phys.* **1990**, 93, 1332.
- (10) Adams, J. E.; Stratt, R. M. *J. Chem. Phys.* **1990**, 93, 1632.
- (11) Bembek, S. D.; Laird, B. B. *Phys. Rev. Lett.* **1995**, 74, 936.
- (12) Kar, S.; Chakravarty, C. *J. Phys. Chem. B* **2000**, 104, 709.
- (13) Rajappa, C.; Bandyopadhyay, S.; Yashonath, S. *Bull. Mater. Sci.* **1997**, 20, 845.
- (14) Krishnan, S. H.; Ayappa, K. G. *J. Chem. Phys.* **2004**, 121, 3197.
- (15) Powles, J. G. *Mol. Phys.* **1983**, 48, 1083.
- (16) Heyes, D. M.; Powles, J. G. *Mol. Phys.* **1990**, 71, 781.
- (17) Israelachvili, J. N. *Intermolecular and Surface Forces: with Applications to Colloidal and Biological Systems*; Academic: London, 1985.
- (18) Seeley, G.; Keyes, T.; Madan, B. *J. Phys. Chem.* **1992**, 96, 4074.
- (19) Boon, J.; Yip, S. *Molecular Hydrodynamics*; Dover Publications Inc.: New York, 1991.
- (20) Balucani, U.; Zoppi, M. *Dynamics of the Liquid State*; Clarendon Press: Oxford, U.K., 1994.
- (21) Haile, J. M. *Molecular Dynamics Simulation*; John Wiley and Sons: New York, 1992.
- (22) Zwanzig, R.; Ailwadi, N. K. *Phys. Rev.* **1969**, 182, 280.
- (23) Madan, B.; Keyes, T.; Seeley, G. *J. Chem. Phys.* **1991**, 94, 6762.
- (24) Pal, S.; Vishal, G.; Gandhi, K. S.; Ayappa, K. G. *Langmuir* **2005**, 21, 767.
- (25) Faeder, J.; Ladanyi, B. M. *J. Phys. Chem. B* **2000**, 104, 1033.



- (26) Ghatak, C.; Ayappa, K. G. *Phys. Rev. E* **2001**, 64, 051507.
- (27) Ayappa, K. G.; Ghatak, C. *J. Chem. Phys.* **2002**, 117, 5373.
- (28) Nicolas, J. J.; Gubbins, K. E.; Street, W. B. *Mol. Phys.* **1979**, 37, 1429.
- (29) Magda, J. J.; Tirrell, M.; Davis, H. T. *J. Chem. Phys.* **1985**, 83, 1888.
- (30) Schoen, M.; Cushman, J. H.; Diestler, D. J.; Rhykerd, C. L. *J. Chem. Phys.* **1988**, 88, 1394.
- (31) Schoen, M.; Diestler, D. J.; Cushman, J. H. *J. Chem. Phys.* **1987**, 87, 5464.
- (32) Krishnan, S. H.; Ayappa, K. G. *J. Chem. Phys.* **2003**, 118, 690.